SUPPORTING INFORMATION

Synergistic interfacial electronic modulation of topotactically developed bimetallic CoNiP on NiS nanorods for enhanced alkaline hydrogen evolution reaction

Woldesenbet Bafe Dilebo [a], Meng-Che Tsai [b *], Chia-Yu Chang [c], Habib Gemechu Edao [a], Yosef Nikodimos [a, d], Endalkachew Asefa Moges [a], Keseven Lakshmanan [c], Fikiru Temesgen Angerasa [a], Chemeda Barasa Guta [a], Kassa Belay Ibrahim [e], Yohannes Ayele Awoke [a], Tesfaye Alamirew [a], Wei-Sheng Liao [c], Gidey Bahre Desta [c], Jeng-Lung Chen [f], Wei-Nien Su [c, d, *], Bing Joe Hwang [a, d, f*]

[a] Nano-electrochemistry Laboratory, Department of Chemical Engineering, National Taiwan University of Science and Technology, Taipei City 106, Taiwan

[b] Department of Greenergy, National University of Tainan, Tainan City 70005, Taiwan

[c] Nano-electrochemistry Laboratory, Graduate Institute of Applied Science and Technology, National Taiwan University of Science and Technology, Taipei City 106, Taiwan

[d] Sustainable Electrochemical Energy Development Center, National Taiwan University of Science and Technology, Taipei City 106, Taiwan

[e] Ca' Foscari University of Venice Via Torino 155,30172 Venezia Mestre, Italy

[f] National Synchrotron Radiation Research Center (NSRRC), Hsinchu 30076, Taiwan

Experimental Section

Chemicals and Reagents. Hydrochloric acid (HCl, 37%), Acetone (C_3H_6O, 99.5%,), Ethanol (99.5%,), DI water (18.2 mΩ cm), Cobalt nitrate hexahydrate ($Co(NO_3)_2 \cdot 6H_2O$, 99.02%), Sodium sulfide nonahydrate ($Na_2S.9H_2O$, 98.02%), Dimethylformamide (DMF, 99.8%), Sodium hypophosphite monohydrate ($NaH_2PO_2 \cdot H_2O$, 98.02%), 20 wt% Pt/C (TEC10E50E, Tanaka Kikinzoku Kogyo K. K., Japan), Nafion solution (86–87%) (Aldrich) and Nickel foam (NF, thickness: 1mm) was purchased from Sheng Qiang Co., Ltd. (Jiangsu, China). The chemicals and reagents utilized in this experiment were all of his analytical grade, and no additional purification was performed.

Preparation of CoP/CP and NiP/CP Catalysts

The cleaned carbon paper (1 × 3) cm was immersed in 1 g mL^{-1} Co $(NO_3)_6.6H_2O$ and 1 g mL^{-1} Ni $(NO_3)_6.6H_2O$ for 1 min and dried at room temperature. Afterward, the dried samples and NaH_2PO_2 powder were placed in two porcelain boats, with the NaH_2PO_2 powder positioned upstream in the furnace. The furnace was then heated to 350 °C at a rate of 2 °C/min for 2 hours under an Ar atmosphere, followed by natural cooling to ambient temperature. Finally, the resulting CoP/CP and NiP/CP Catalysts were removed from the furnace once it reached room temperature. In addition, to determine the effects of the NF support in the heterostructured catalyst, bare NF was subjected to phosphorization following the same procedure used to prepare NiP/NF.

Preparation of 20 wt% Pt-C/NF

6.0 mg of commercial 20 wt% Pt/C catalysts were first dissolved in 200 mL of ethanol, 150 mL of water, and 50 mL of Nafion solution using an ultrasonic treatment for 30 minutes to form a homogenous ink. The above-mentioned uniform ink was then gradually dropped onto cleaned NF and dried in air. Pt-C/NF loading is 0.22 mg. Similarly, RuO_2 /NF was prepared using the same

procedure.

Computational details

All DFT calculations in the present work were performed by the Vienna *Ab initio* Simulation Package (VASP) 5.4.4 code[1] with the Perdew-Burke-Ernzerh of (PBE) functional.[2] The ion-electron interaction was described by the projector augmented wave (PAW) method [3] with a cutoff energy of 500 eV. The structural models of Ni_3S_2, Ni_8P_3, and CoP were constructed to calculate the free energy of the reaction intermediates in hydrogen evolution reaction (HER), see Figs. (S17 a-c). To match the experimental observation, the crystalline facets that are more likely to be exposed on the surface are selected. For example: Ni_3S_2 (110), Ni_8P_3 (100), and CoP (011). A Monkhorst-Pack *k*-point mesh with a size of 3 × 3 × 1 [Ni_3S_2 (110) and CoP (011)] and 5 × 3 × 1 [Ni_8P_3 (100)] and the spin polarization was applied for the calculations. Additionally, CoP/Ni_3S_2 (110) and Ni_8P_3/Ni_3S_2 (110) surface models were constructed to investigate the effect of hetero-structure in HER (Figs. S17 d-e). Furthermore, the DFT-D_3 correction method in Grimme's scheme[4, 5] was used to accurately describe the long-range vdW interactions. All the calculations were carried out until the total energy and force were less than 10^{-5} eV per atom and 0.05 eV $Å^{-1}$, respectively.

The calculation of the free energy for the reaction intermediates was performed by an equation: $G = E_{DFT} + ZPE - TS$, where E_{DFT} is the total energy, ZPE is the zero-point energy, T is the temperature in Kelvin, and S is the entropy. Calculating the vibrational frequencies in the harmonic normal-mode approximation determines the value of ZPE. The free energy diagram in the HER can be obtained according to its reaction mechanism. The first step is the formation of a hydroxyl group. Its free energy is defined as:

$$\Delta G_{OH} = G_{OH*} - G_{*} - G_{H_2O} + \frac{1}{2} G_{H_2}$$

Second, the free energy of hydrogen adsorption can be defined as:

$$\Delta G_H = G_{H*} - G_* - \frac{1}{2} G_{H_2}$$

Estimation of Electrochemical Active Surface Area

Through cyclic voltammetry (CV) measurement with various scan rates (v) in non-faradaic regions, the electrochemical double-layer capacitance (C_{dl}) was computed to determine the electrochemical surface area (ECSA). The double layer capacitance (C_{dl}) is obtained by plotting half of the positive and negative current density differences ($j = j_a - j_c/2$) at a particular potential against the CV scan rates, which is equal to the value of the linear slopes of the plot. Using the specific capacitance value for a flat standard with a real surface area of 1 cm^2, the C_{dl} can be transformed into an electrochemical active surface area (ECSA). A flat surface's specific capacitance is typically reported to range between 20 and 60 F cm^{-2}.[6-8] We use a 40 μFcm^{-2} assumption to calculate ECSA. Equation (S1) can be used to compute the ECSA:

$$A_{ECSA} = \frac{C_{dl}\ of\ catalyst\ (mF\ cm^{-2})}{0.04\ mF\ cm^{-2}\ per\ cm^2_{ECSA}} \quad \text{(S1)}$$

Site activity (SA)

In catalysis refers to the intrinsic activity of a specific catalytic site or active site on a catalyst surface. It represents the ability of a single active site to catalyze a reaction. The term is often used in heterogeneous catalysis because, in a heterogeneous catalytic reaction occurring on a metal surface, different sites on the surface may have varying levels of activity due to differences in their electronic structure or accessibility. [9, 10] This can be calculated by applying the following Equation (S2),

$$SA = \frac{j\eta = 110\ mV}{Cdl} \quad \text{(S2)}$$

Where j_η, is the current density at the specific overpotential.

The LSV curves were recorded at a scan rate of 2 mV s^{-1} to obtain polarization curves with iR compensation. The iR correction was carried out by Equation (S3)

$$E_{Corrected} = E_{RHE} - iRs \quad (S3)$$

where i and Rs are current and equivalent series resistance, respectively.

The Faradaic efficiency (FE) of the sample was measured to analyze the H_2 produced at a current density of 50 $mAcm^{-2}$. Faradaic efficiency was acquired from Equation (S4)

$$FE = \frac{(V \; x \; n \; x \; F)}{(I \; x \; t \; x \frac{24.5L}{mol})} \quad (S4)$$

where V is the volume of H_2, n is the number of electrons transferred, F is the Faraday constant, I is the current value, and t (s) is the electrolysis time.

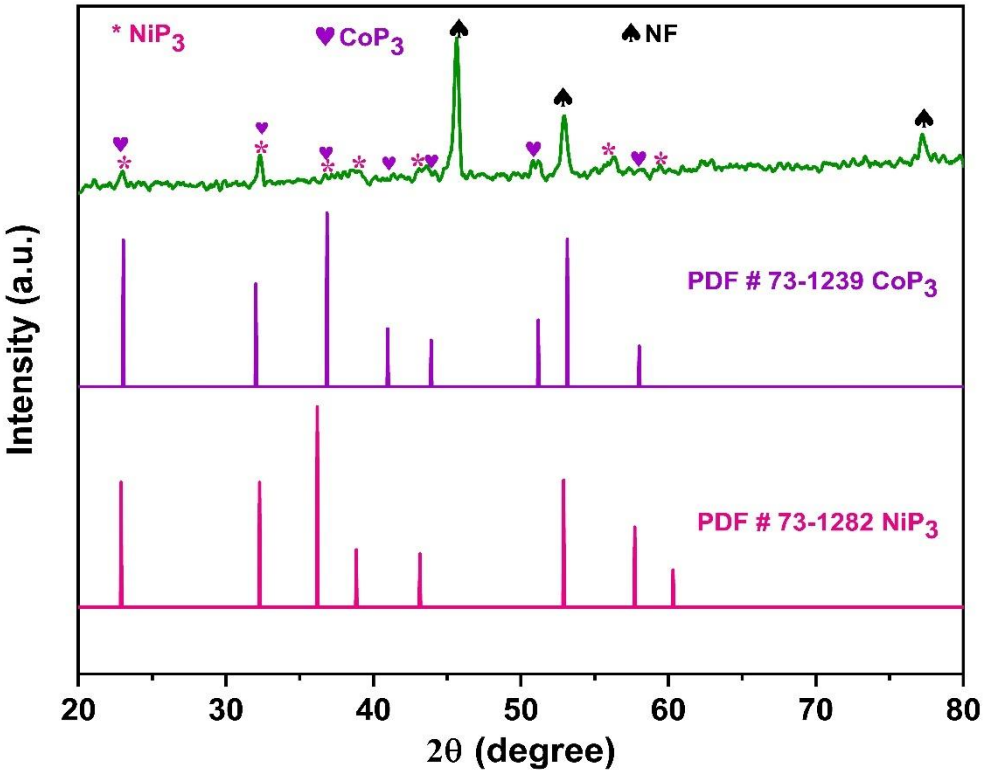

Fig. S1. XRD pattern of CoNiP/NF with references.

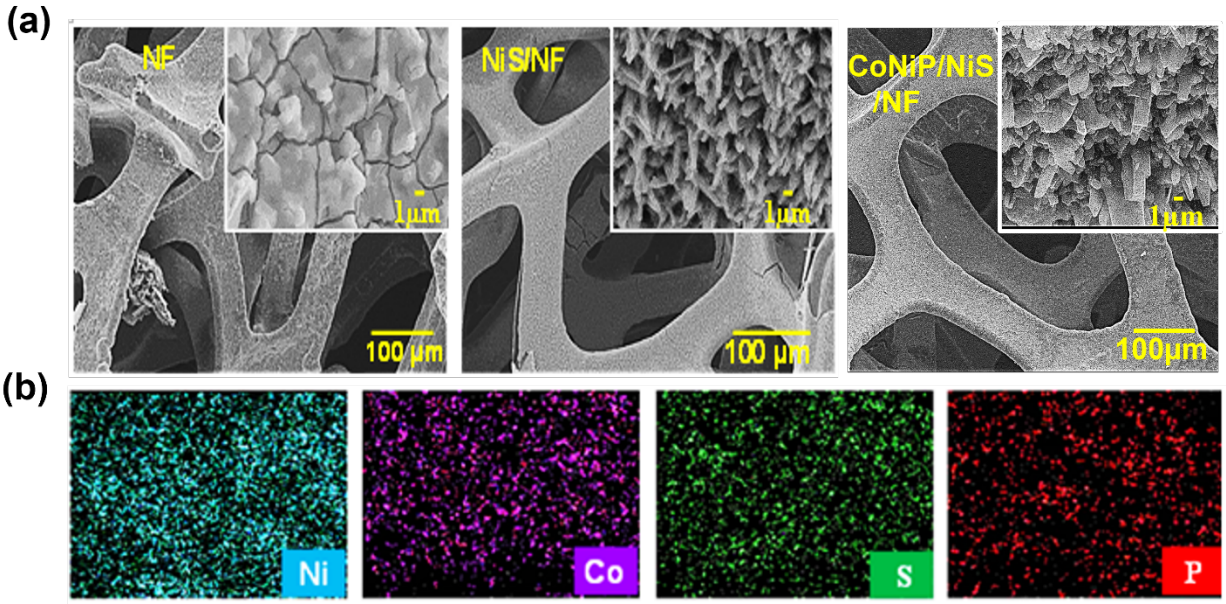

Fig. S2. (a) Typical SEM images of NF, NiS, and CoNiP|NiS/NF catalysts respectively at different magnifications, **(b)**. EDX mapping for each element of CoNiP/NiS/NF heterostructure.

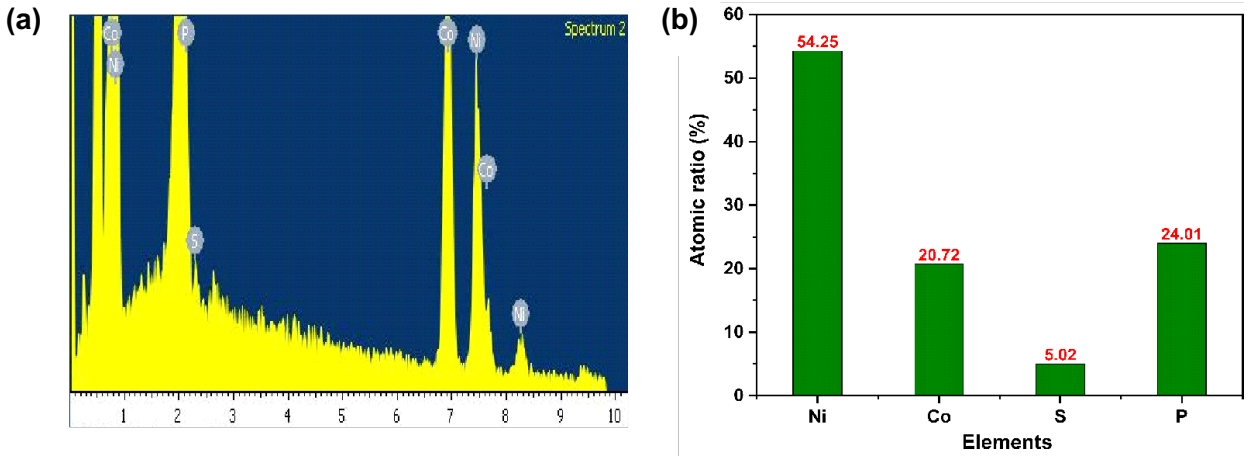

Fig. S3. (a, b) EDX spectra and atomic ratios for CoNiP/NiS/NF heterostructure.

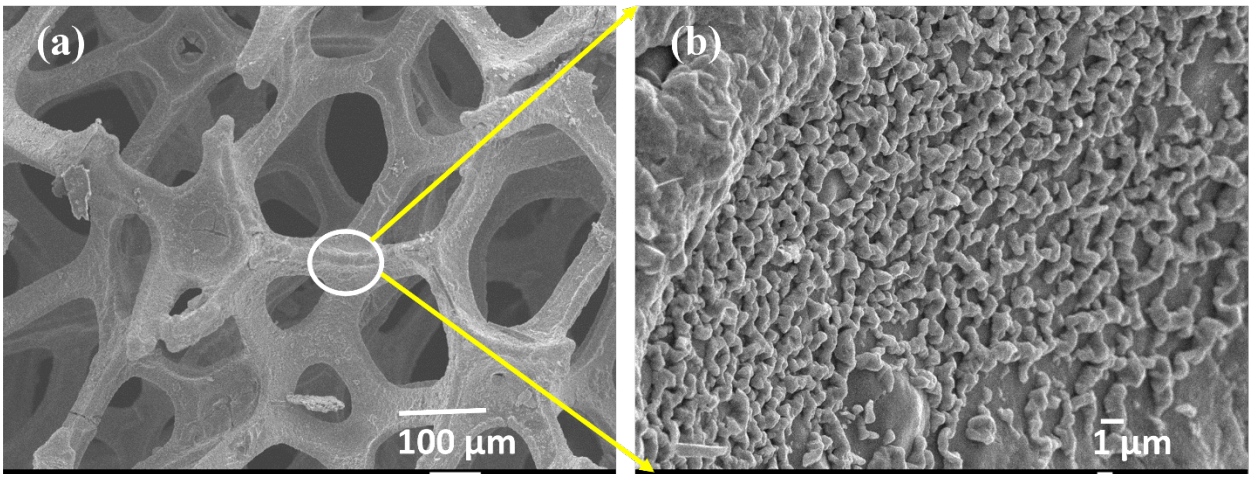

Fig. S4. (a, b) Scanning electron microscope (SEM) images of CoNiP/NF at different magnifications.

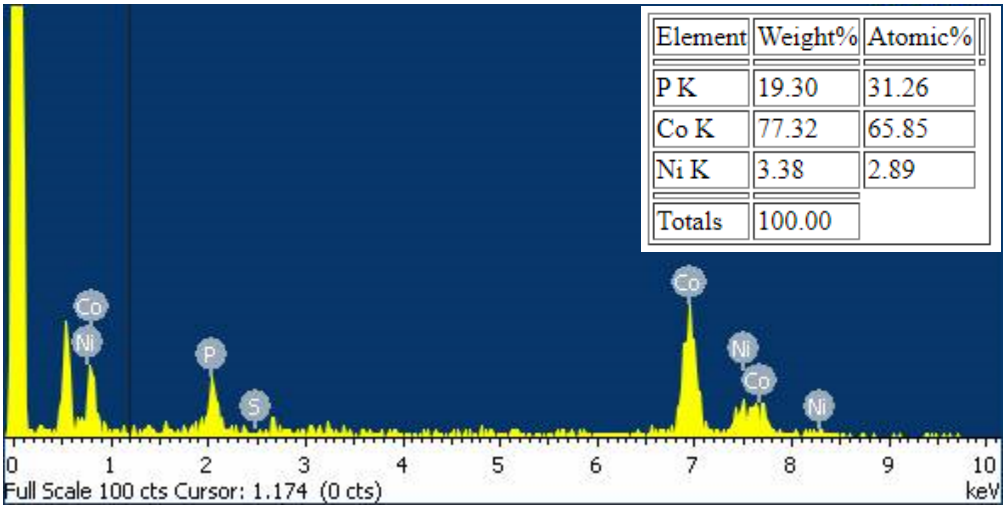

Fig. S5. EDX spectrum and atomic ratio of each element for heterostructure CoNiP/NF.

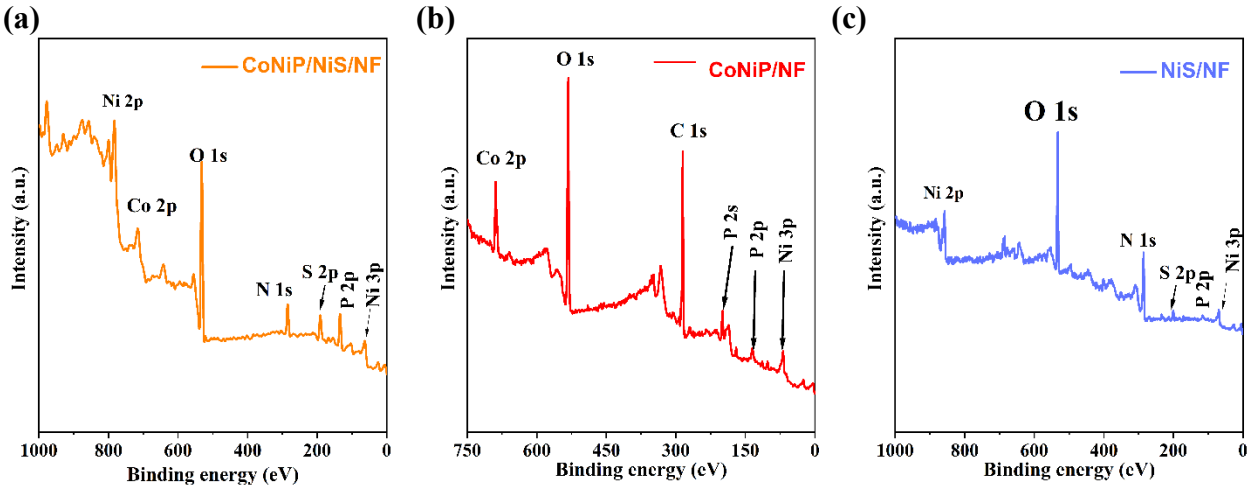

Fig. S6. XPS survey spectra for **(a)** CoNiP/NiS/NF, **(b)** CoNiP/NF and **(c)**. NiS/NF

Supplementary Discussion 1 | In-situ Raman spectra

After applying cathodic potential, the typical Raman active mode of Co-P bond stretching in the CoNiP/NiS/NF electrode around 523 cm^{-1} was broadened. The peak around 681 cm^{-1} overlapped with the near Ni-O bond and almost vanished (Fig. S7b). These indicate that the adsorption of hydroxide species on the electrode surface can modify the electronic structure of CoP bonds and transfer them to another phase due to the CoOOH or Co-O stretching modes the alkaline electrolyte.[11, 12] However, this feature is not observed for the CoNiP/NF electrode (Figs. S7c, d), indicating there is a strong electronic interaction between CoNiP and NiS species on the surface of the CoNiP/NiS/NF electrode.[13] In addition, the decline of the intensity between the range of 290 cm^{-1} and 336 cm^{-1} probably indicates the adsorption of OH* from the electrolyte on the surface of NiS and NiP species. All this suggested that the surface electronic interactions are more sensitive for activation of water molecules. The in-situ Raman analysis was conducted in a 1 M KOH electrolyte using the specially designed setup illustrated in Fig. S7e.

The catalytic activities of TMPS are closely related to their surface features and species. Under the HER process, alkaline electrolytes undergo an electrochemical reconstruction into corresponding species.[14, 15] This in-situ developed surface species exhibits a strong electrostatic affinity to the local environments and facilitates the reaction by absorbing OH*, which blocks the active sites for H* adsorption.[16] Therefore, these topologically existing species protect the dissolution of the active interface and refresh the active site for HER to proceed.

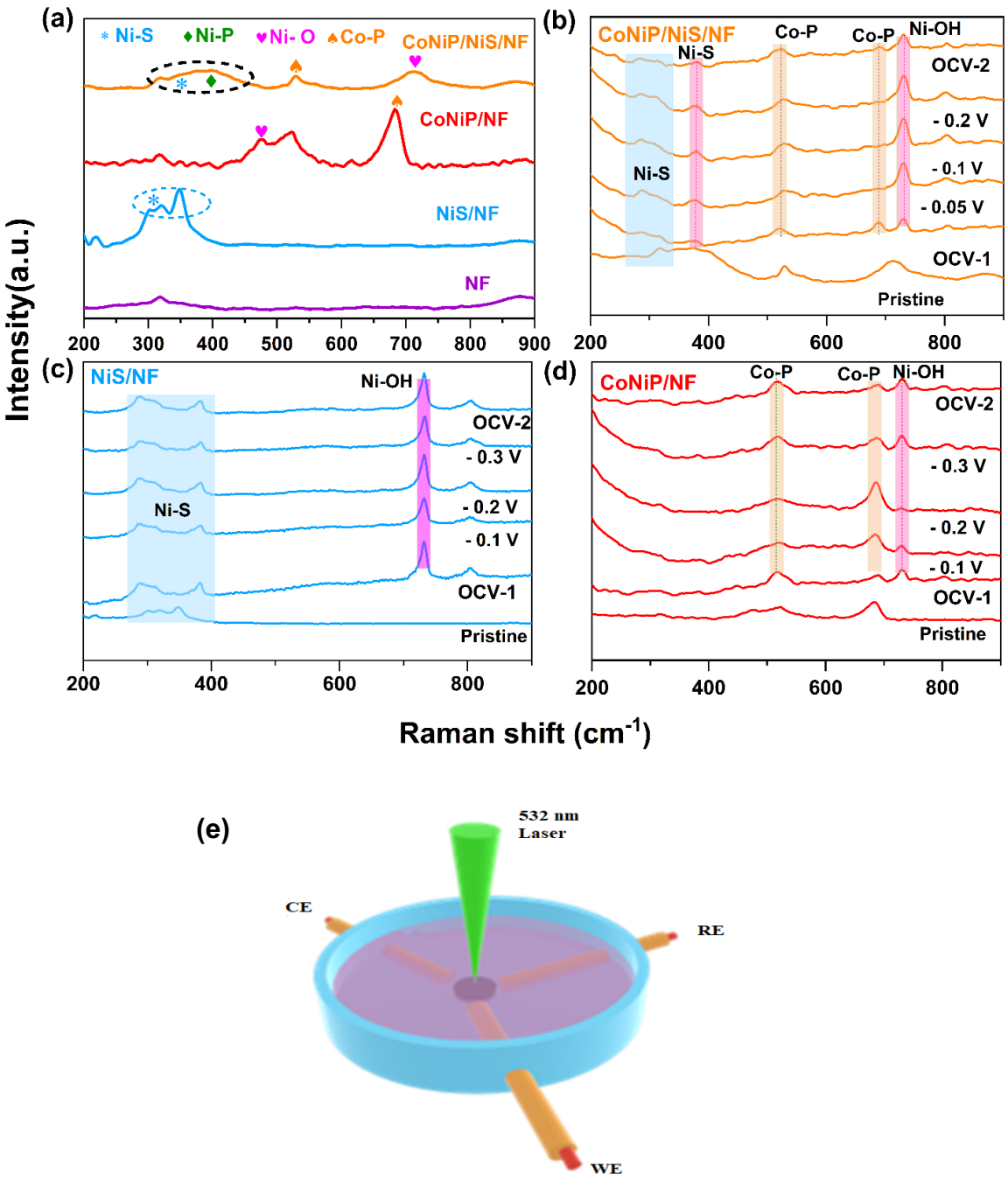

Fig. S7. (a) Ex-situ and In-situ Raman spectra of CoNiP/NiS/NF, CoNiP/NF, NiS/NF samples**;** In-situ Raman spectra of (b) CoNiP/NiS/NF, (c) NiS/NF, and (d) CoNiP/NF, respectively, with the reaction before any applied potential (OCV-1) and the reaction after any applied potential (OCV-2, (**e)** Scheme of In-situ Raman spectroscopy.

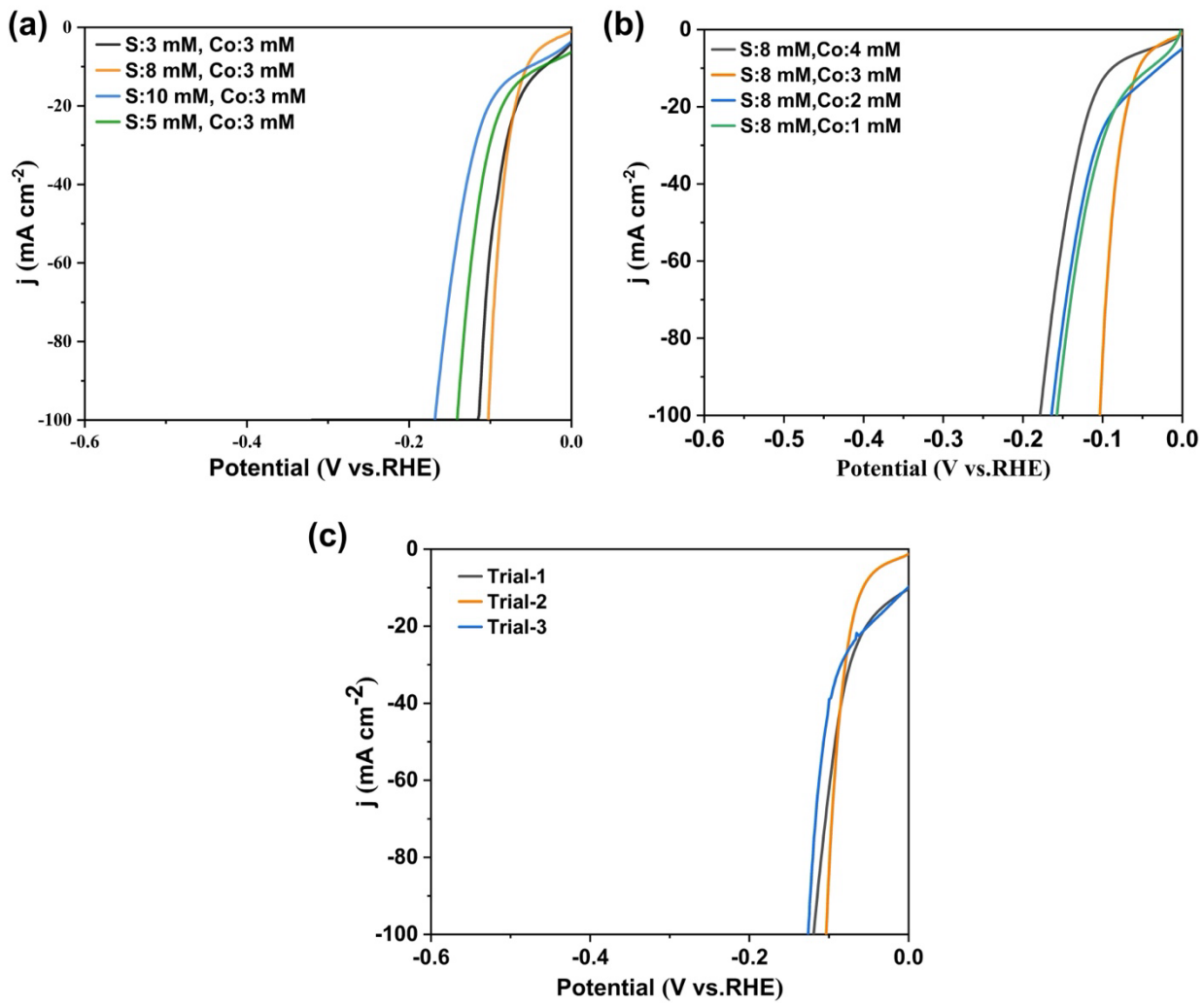

Fig. S8. HER polarization curves of CoNiP/NiS/NF with various amounts of (a) S and (b) Co precursors and (c) reproducibility of the sample at different trials.

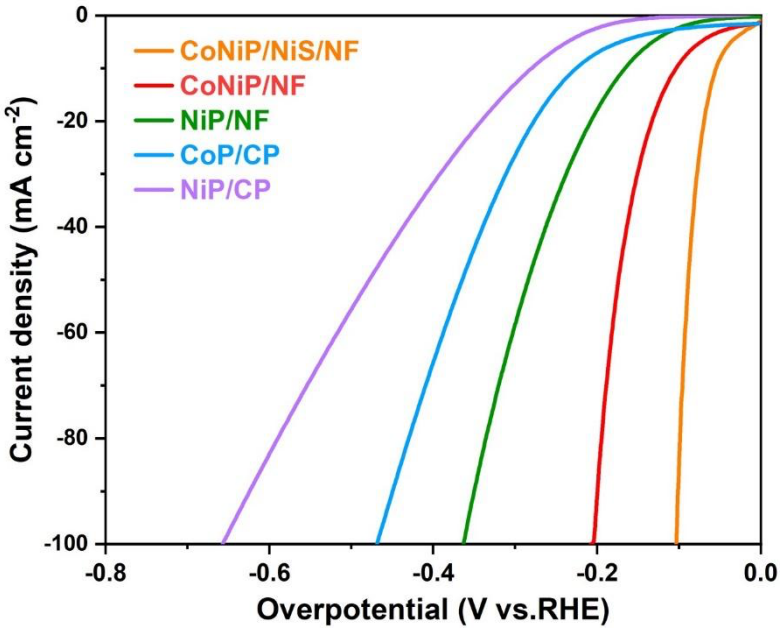

Fig. S9. Polarization of HER curves of NiP/CP and CoP/CP, NiP/NF, CoNiP/NF, CoNiP/NiS/NF electrodes.

Estimating turnover frequency (TOF)

Turnover frequency (TOF) is a measure of catalytic activity that quantifies the number of times a catalytic site on a catalyst surface participates in a chemical reaction per unit time. It is typically expressed in units of moles of product formed per mole of active sites or catalyst per second (mol/s/mol or s^{-1}). It provides information about the rate at which a catalyst can facilitate the conversion of reactants into products. The equation provided was used to calculate the turnover frequency (TOF) and the density of active catalysts sites. It was assumed that all active sites were completely exposed to the electrolyte.

The number of voltammetric charges (Q) can be determined by the integral area, n could be determined with the following equation,

$$n' = \frac{Q}{2nF} \quad \text{(S5)}$$

$$TOF = \frac{J.A}{2n'F} \quad \text{(S6)}$$

where J is the cathodic current density (A cm^{-2}) at specific overpotential, A is the area of the electrode, F is the Faraday constant (96,485 C mol^{-1}), and n (mol) is the number of moles of the active materials, which was examined employing cyclic voltammograms with 1 M KOH at a scan rate of 50 mV s^{-1}.

The TOF values that varied with various overpotentials are displayed in Fig. S10, and the values are 5.43, 2.80, 2.30 and 1.18 s^{-1} for CoNiP/NiS/NF, CoNiP/NF, NiS/NF, and NF catalysts at the overpotential of 85 mV, respectively.

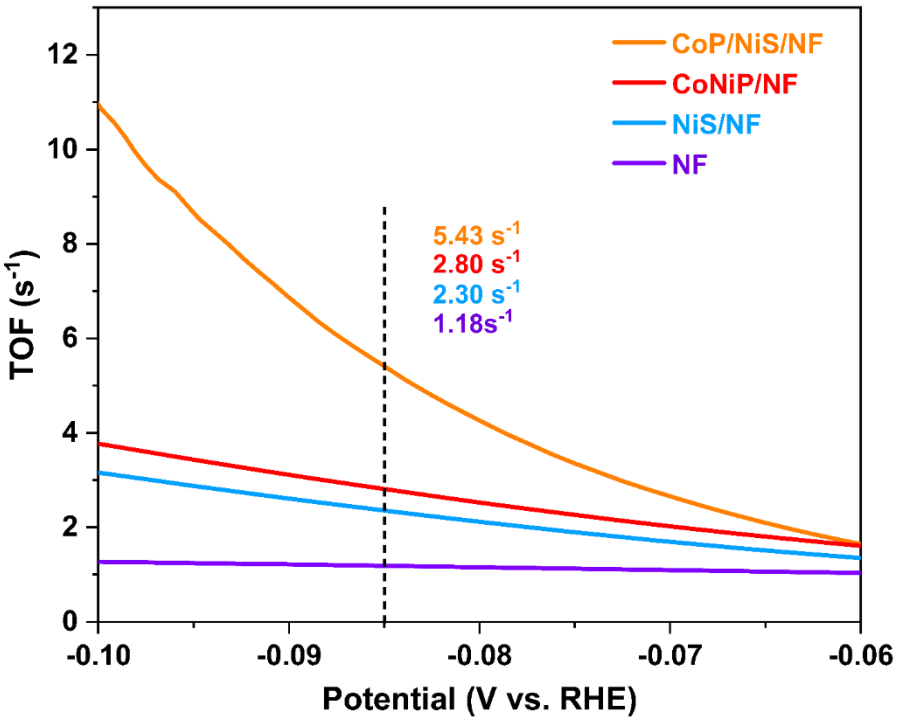

Fig. S10. Calculated H_2 turnover frequencies (TOFs) of different catalysts.

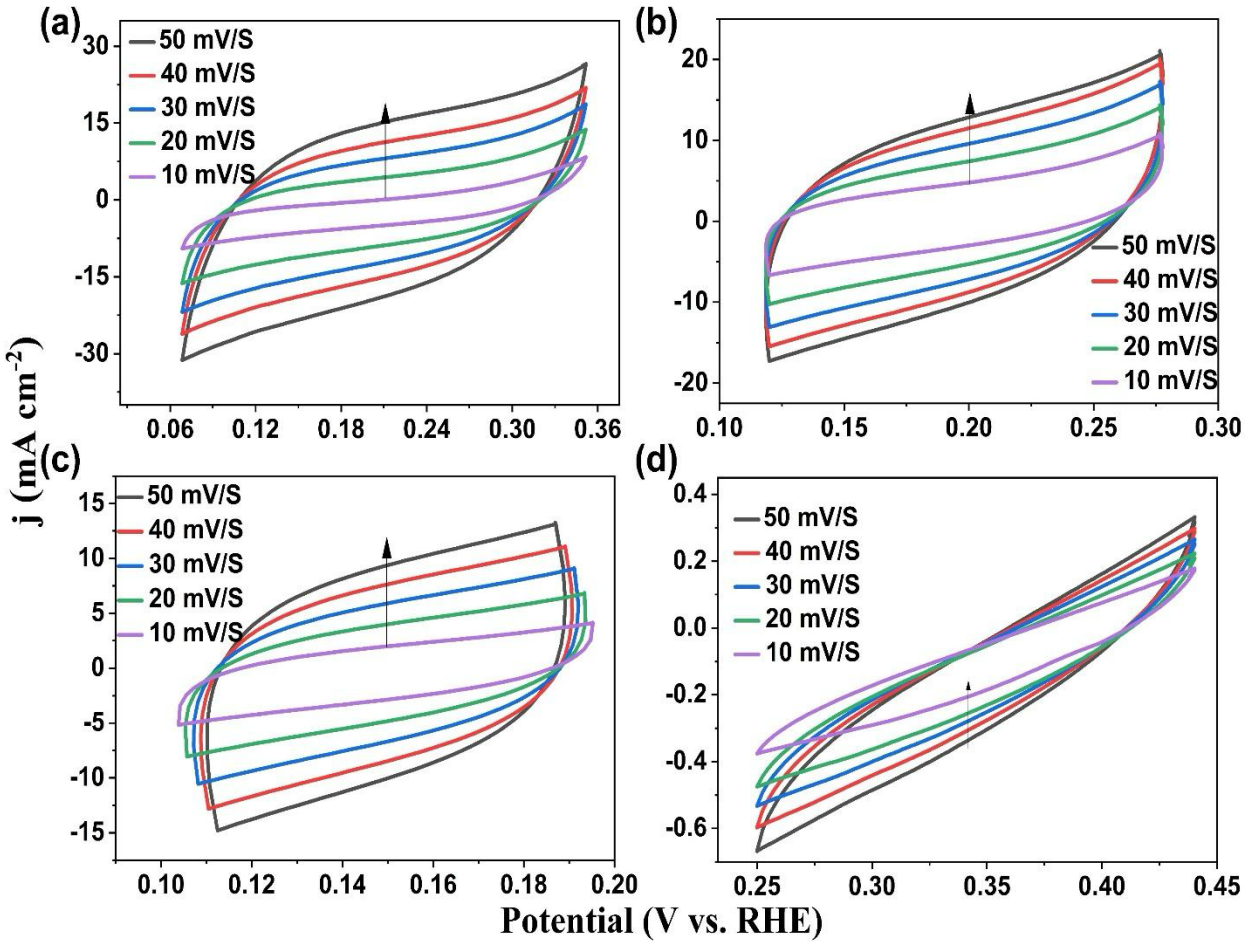

Fig. S11. CV graphs for (a). CoNiP/NiS/NF, (b) CoNiP/NF, (c) NiS/NF, and (d) NF at different scan rates in 1.0 M KOH purged with Ar.

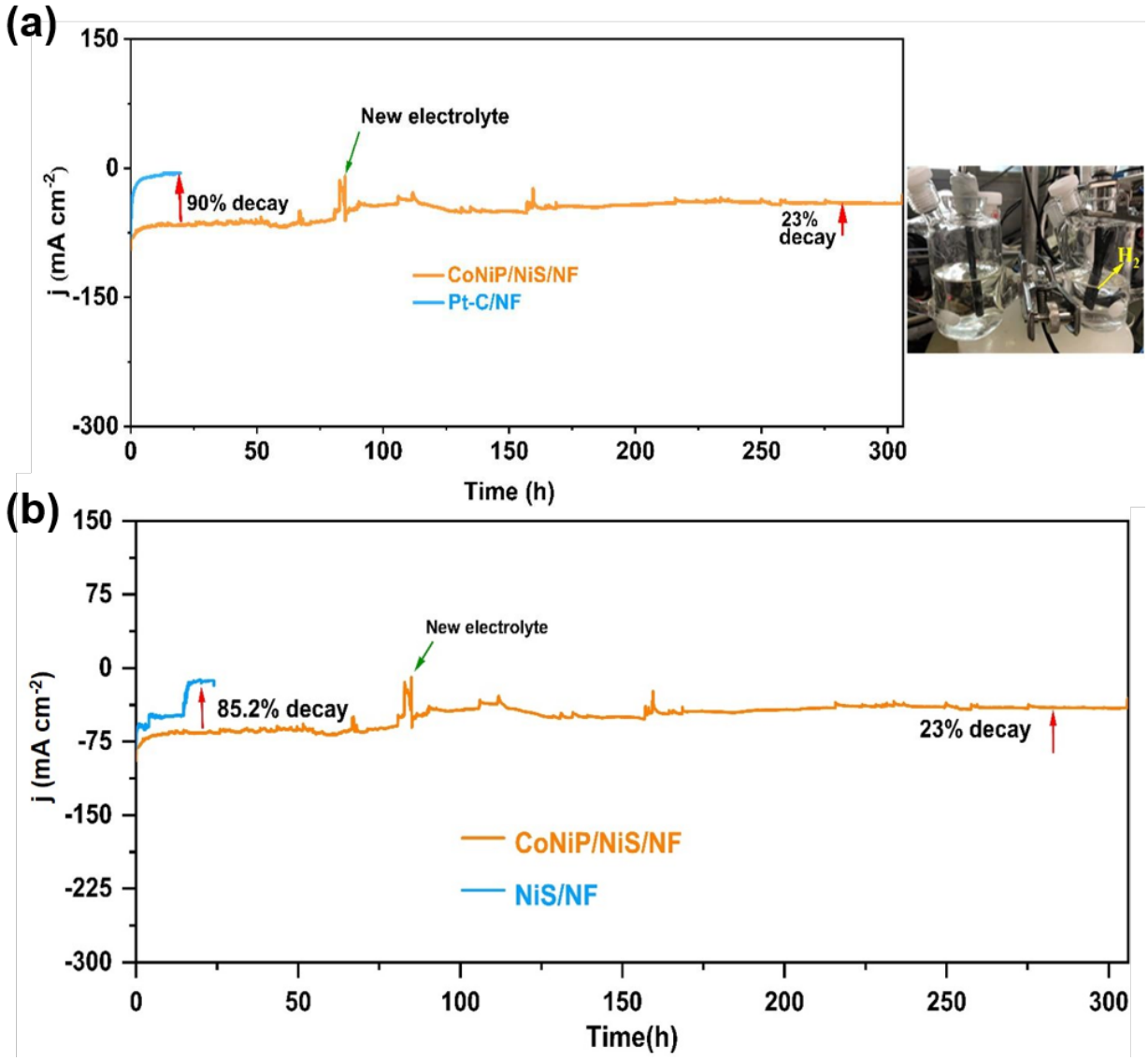

Fig. S12. Comparison of chronoamperometric responses of (a), CoNiP/NiS/NF with Pt-C/NF and, (b), CoNiP/NiS/NF with NiS/NF catalyst.

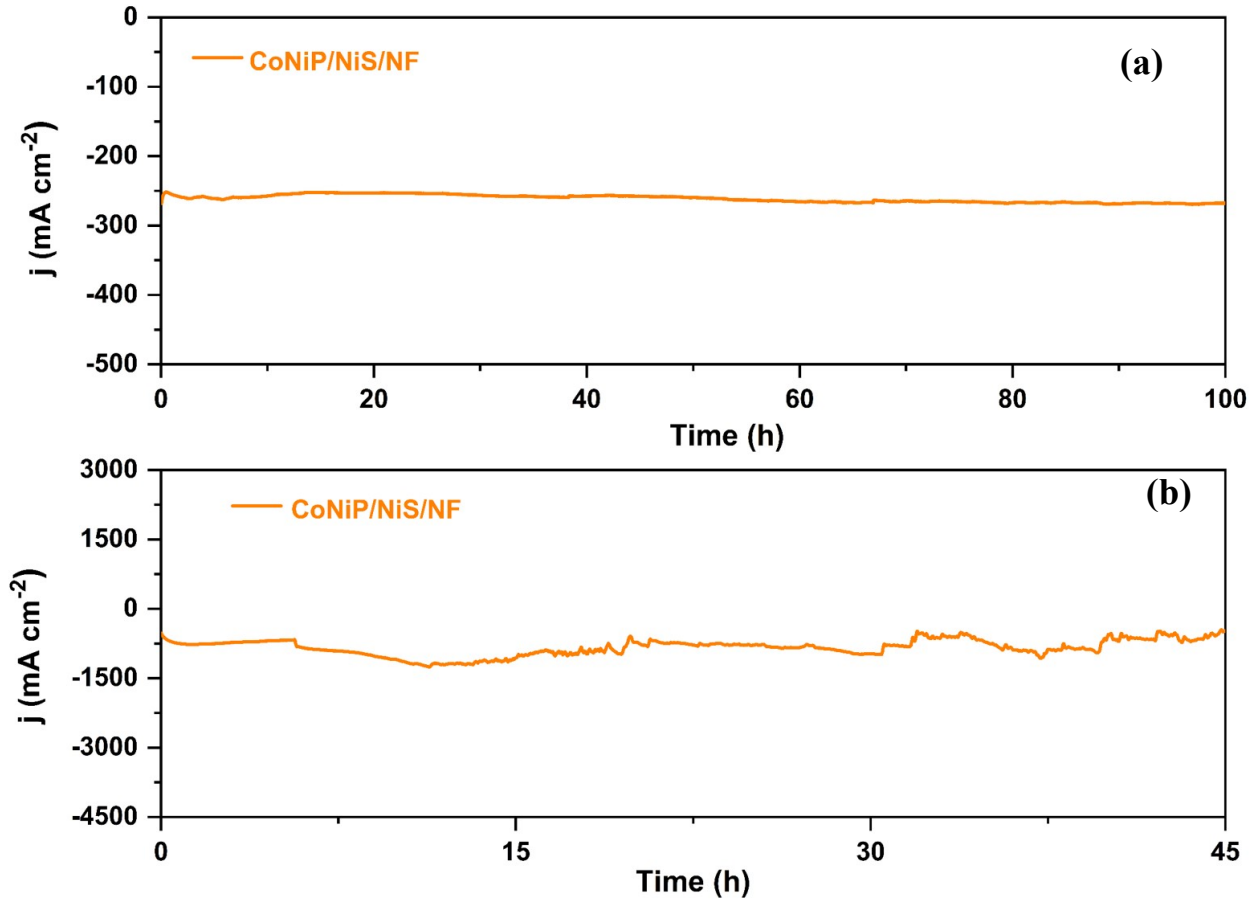

Fig. S13. Chronoamperometric responses of CoNiP/NiS/NF at high current density values (a) -0.25V, and (b) -0.5V.

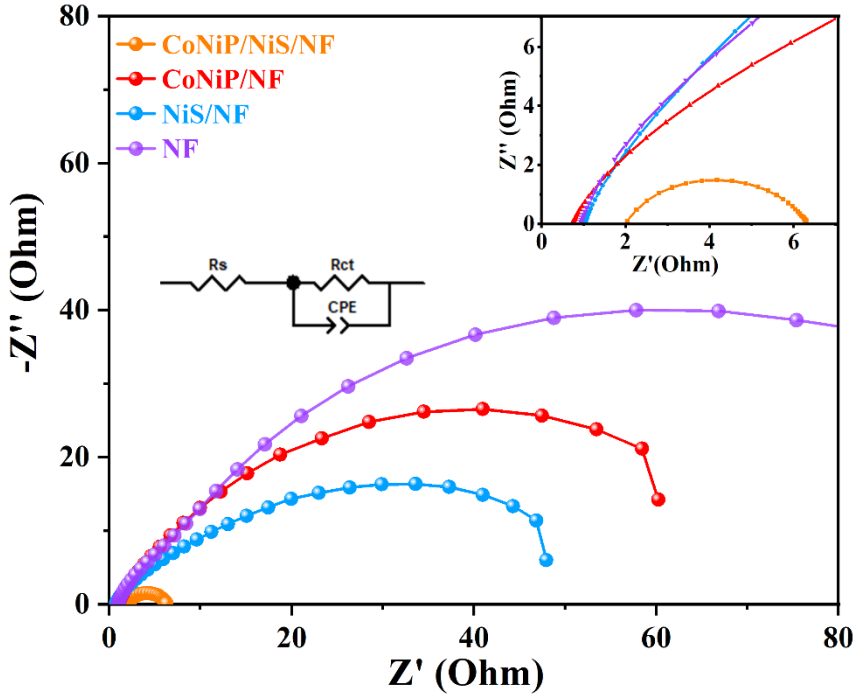

Fig. S14. Nyquist plots of CoNiP/NiS/NF, CoNiP/NF, and NiS/NF catalysts at the overpotential of 51 mV.

Supplementary Discussion 2 | Overall Water Splitting

Motivated by the outstanding activities of the CoNiP/NiS/NF catalyst in alkaline HER, we implemented a water-splitting cell setup (Fig. S15a). The setup involves utilizing CoNiP/NiS/NF as the cathode and RuO_2/NF as the anode to evaluate their combined efficiency in water splitting. In Fig. S15b, the polarization curve was obtained by measuring 5 mV s^{-1} scan rate. Interestingly, the electrode has a low 1.47 V onset potential. It generates a current density of 75mA cm^{-2} at a remarkably low voltage of 1.55 V. These values are superior to those observed for other catalysts. The outstanding efficiency in overall water electrolysis can be ascribed to the successful integration of OER and HER facilitated by the hierarchical 3D-networked structures.

Furthermore, to assess the stability of the cell system, the ongoing operation was conducted for 24 hours at 1.55 V. As shown in Fig. S15c, the CoNiP/NiSNF demonstrated remarkable stability during long-term testing without any deactivation in current density, indicating excellent electrochemical stability. This suggests that the system is highly suitable for practical large-scale applications. In conclusion, the CoNiP/NiS/NF (-) || RuO_2 (+) cell system exhibits exceptional design characteristics for practical water-splitting applications due to its high activity and long-term durability.

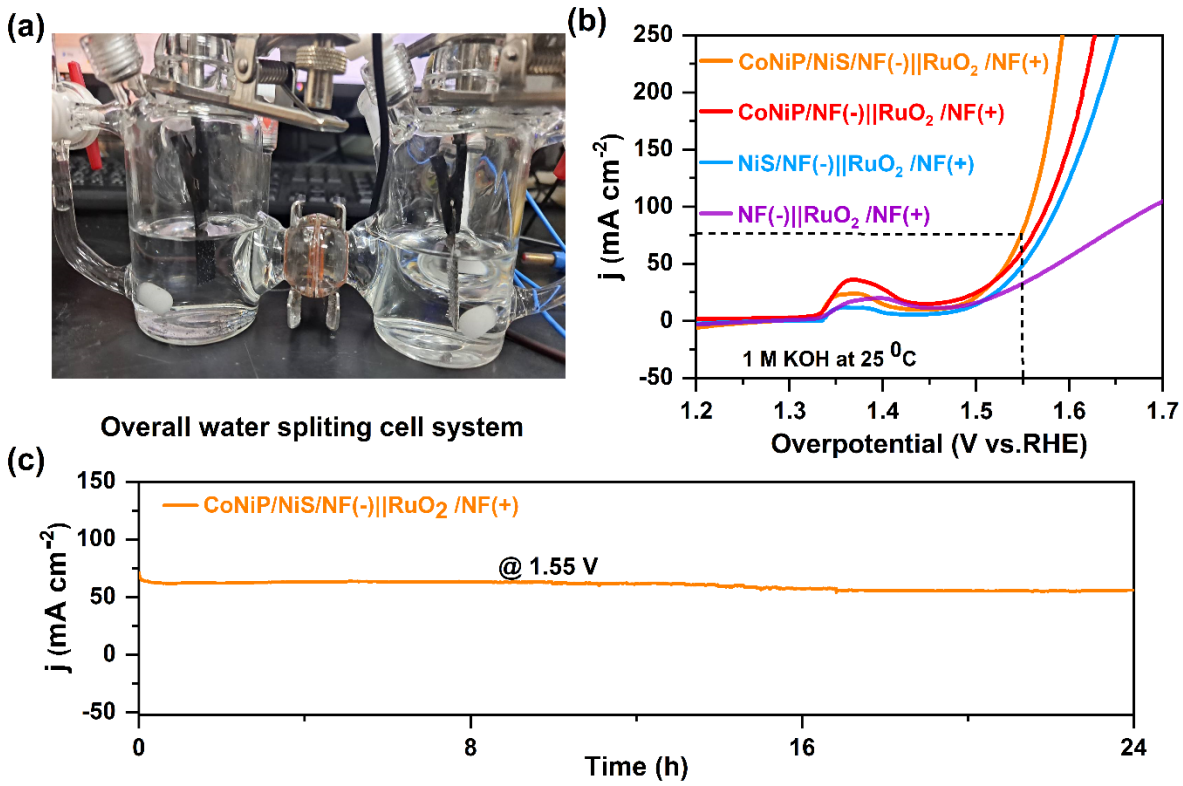

Fig. S15. (**a**) Photograph of an overall water splitting cell system with a 1.55 V at room temperature. **(b)** Polarization curves for the CoNiP/NiS/NF (-) || RuO_2/NF (+) cell system for overall water splitting in 1 M KOH. **(c)** Durability test without iR correction for the CoNiP/NiS/NF (-) || RuO_2/NF (+) cell system at a cell voltage of 1.55 V.

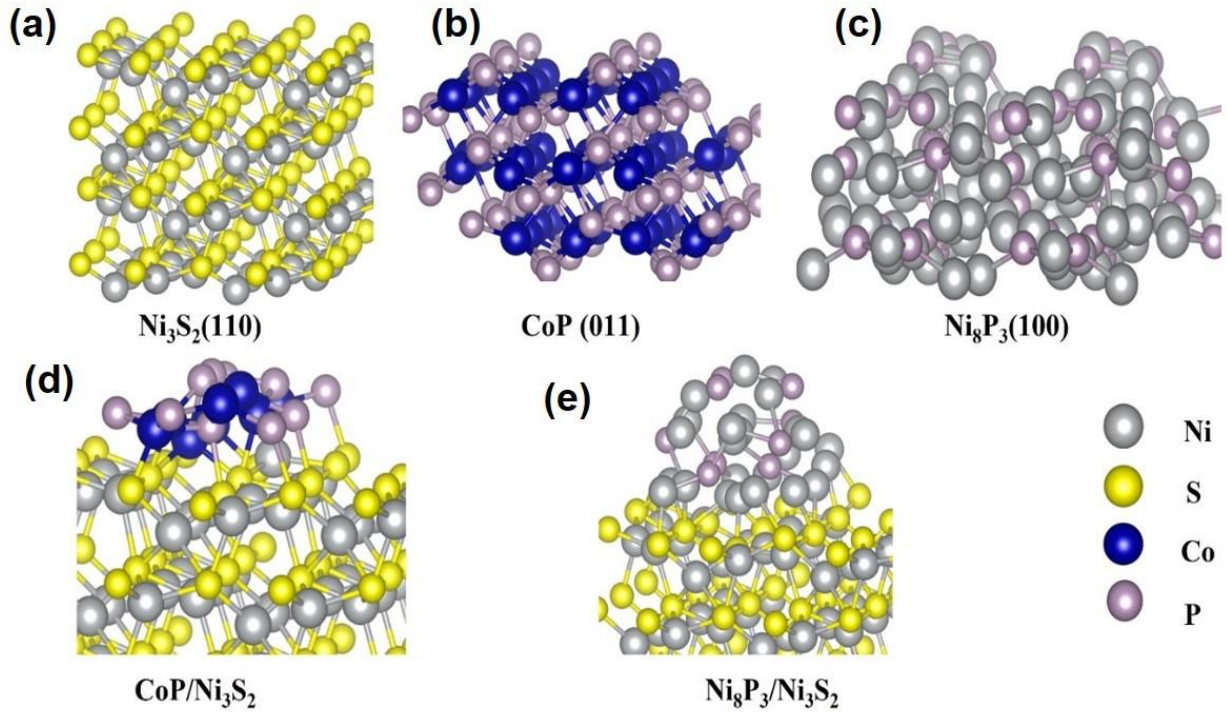

Fig. S16. Structural models of **(a)** Ni_3S_2 (110), **(b)** CoP (011), **(c)** Ni_8P_3 (100), **(d)** CoP/Ni_3S_2 (110) and **(e)** Ni_8P_3/Ni_3S_2 (110). Silver, yellow, blue, and purple balls are Ni, S, Co, and P atoms.

Supplementary Discussion 3 | Post-characterization of hierarchical electrocatalysts

As the SEM image illustrates in Fig. S17a, the nanorods structure morphology is preserved after the aging test; however, the smooth surface of nanorods has become rougher. This is due to the dissolution of surface material in an alkaline solution during the release of H_2 gas. [17] Elemental mappings of SEM-EDS results show a uniform distribution of Co, Ni, P, and S after aging (Figs. S17b, and S17c).

Similarly, the crystal structure analyzed by the XRD pattern after passing a long-term durability test is almost comparable to that of the pristine one (Fig. S18). Additionally, the XPS analysis of the survey spectrum after the aging is displayed in Fig. S19, which shows the presence of elements Co, Ni, P, and S that are distributed uniformly. As demonstrated in Figs. S20a-d, the valence states of all species do not show noticeable changes after the HER aging. This indicates that the prepared electrode has higher surface stability.

After aging, the O_{1s} spectrum shows that peak intensity for M-OH is increased, indicating more metal hydroxyl groups on the surface were formed. The increased intensity of hydroxyl groups is accompanied by the decrease of SOx/PO_x peak (Figure S21), illustrating that the surface species have been performed for catalyzing HER.

The atomic ratio of each element before and after aging is displayed in (Fig. S22) and it reveals an increase of oxygen element, indicating that more oxygen was adsorbed from the electrolyte solution.

In addition, the surface structure, coordination environment, composition, and oxidation state after aging were displayed in Figs. S23a and S23b. The results reveal that the electrodes display a lower intensity profile after aging than the pristine. This could indicate that the electrodes have higher electron density due to the adsorption -OH* group from the electrolyte. Overall, the post-

characterization findings offer enough proof that the prepared CoNiP/NiS/NF hetero-structure electrode maintains its structure during HER without the catalyst appearing to deactivate or detach from the electrode surface.

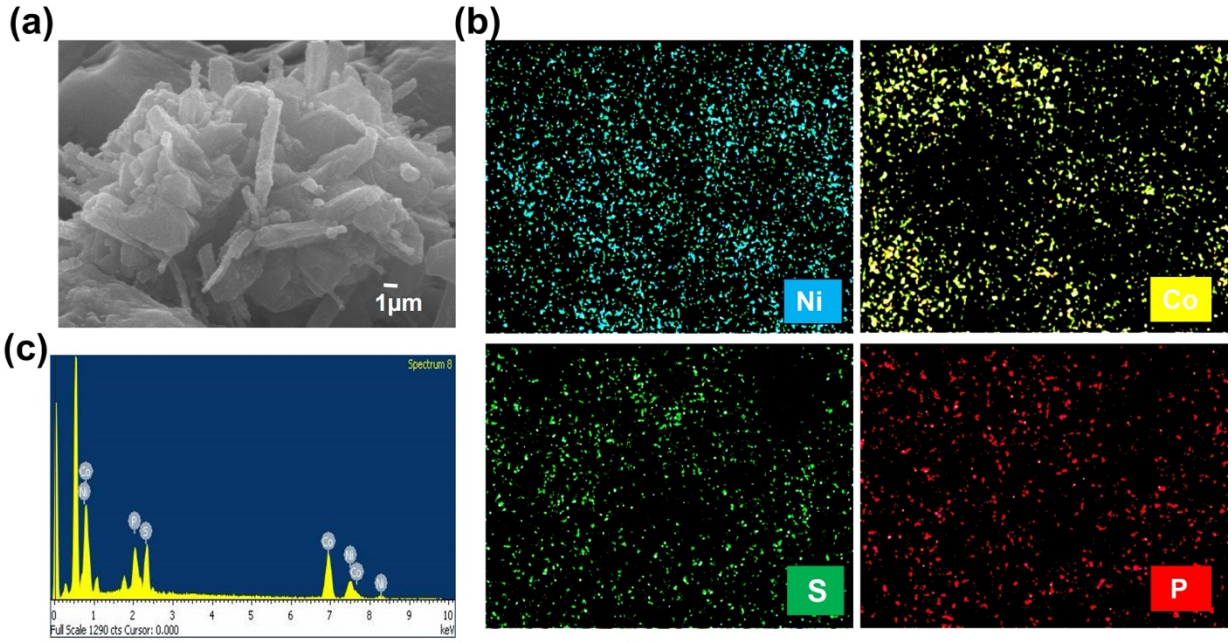

Fig. S17. (a). SEM image, **(b).** Elemental mapping distribution, **(c).** EDS results of S, P, Co and Ni after aging at scale bar: 1 μm of CoNiP/NiS/NF.

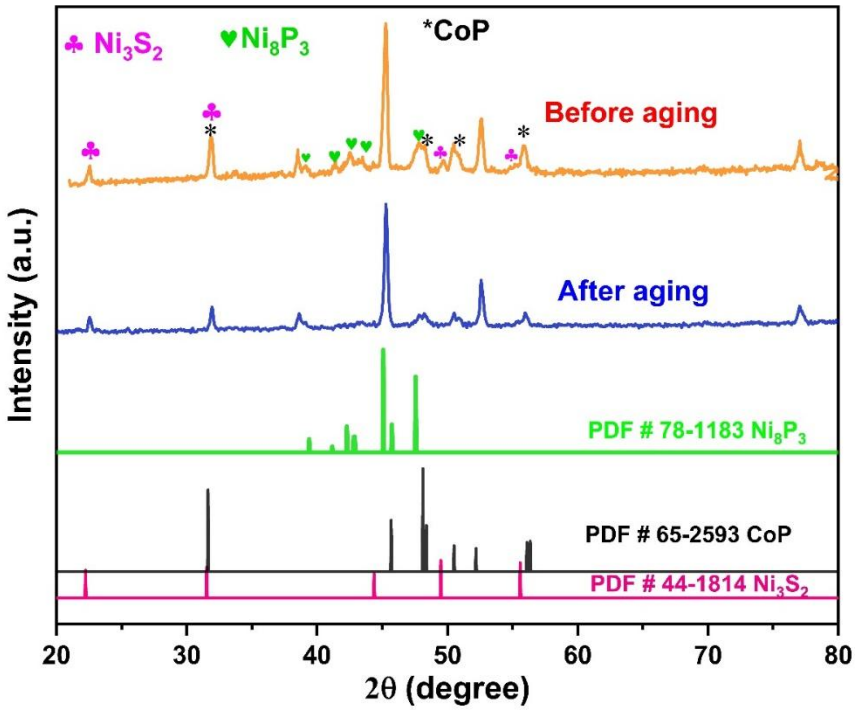

Fig. S18. XRD patterns of CoNiP/NiS/NF before and after the aging.

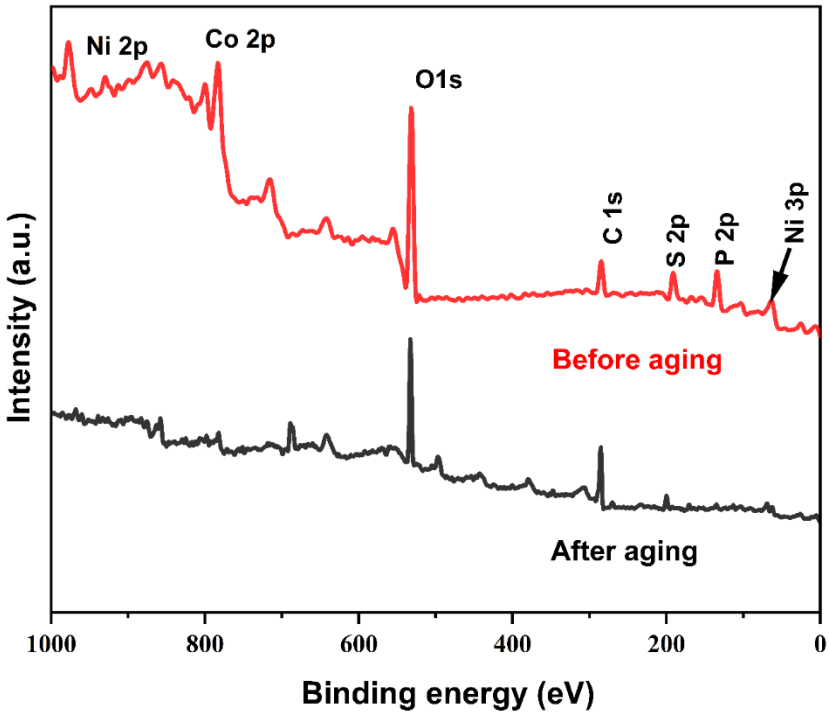

Fig. S19. XPS Survey spectra for CoNiP/NiS/NF before and after the aging.

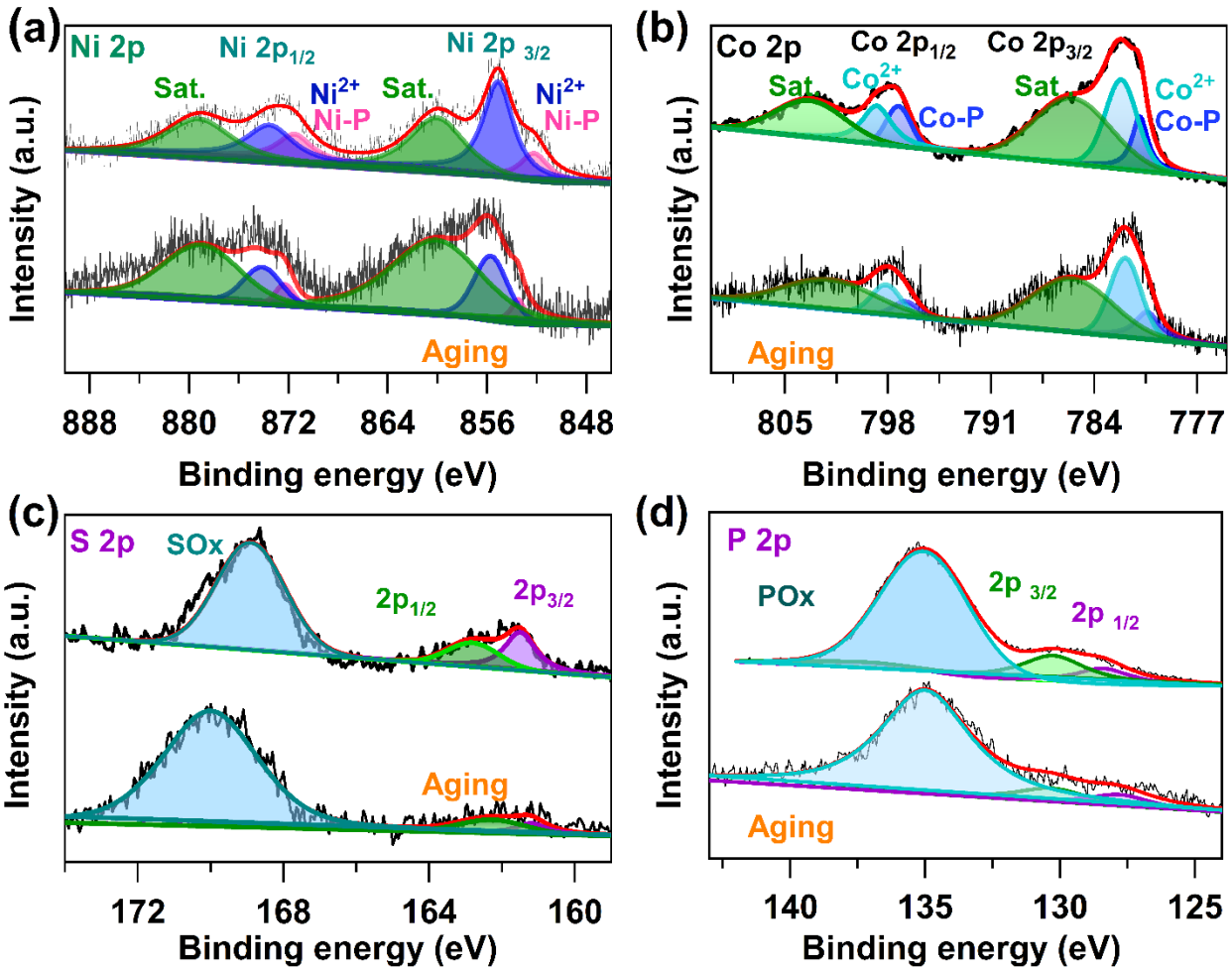

Fig. S20. Core-level XPS of before aging and aging for (a) Ni 2p, (b) Co 2p, (c) S2p, (d) P 2p spectra for CoNiP/NiS/NF.

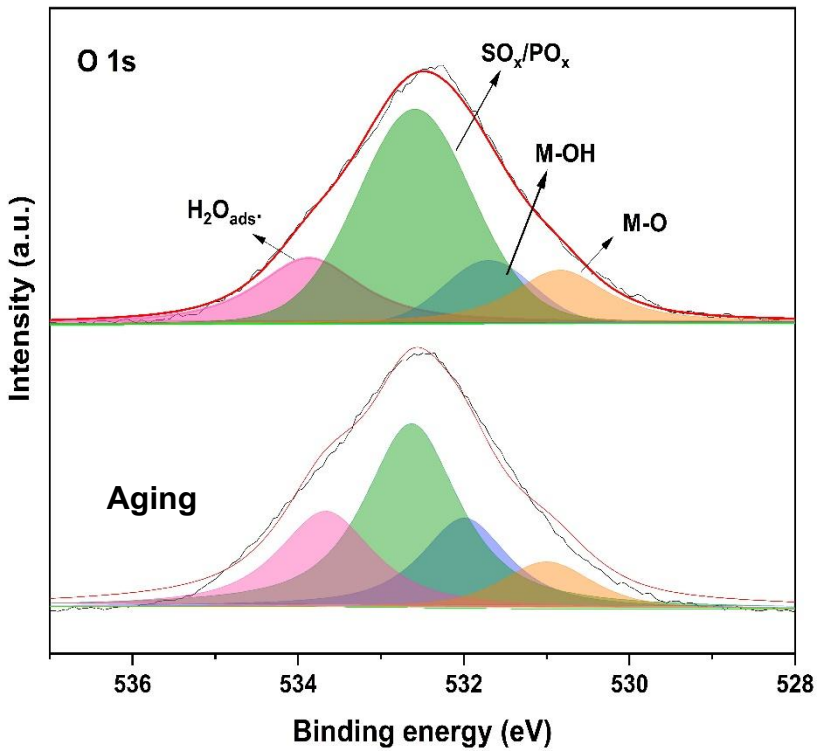

Fig. S21. O 1s spectra of the CoNiP/NiS/NF heterostructure nanorod electrode before and after aging.

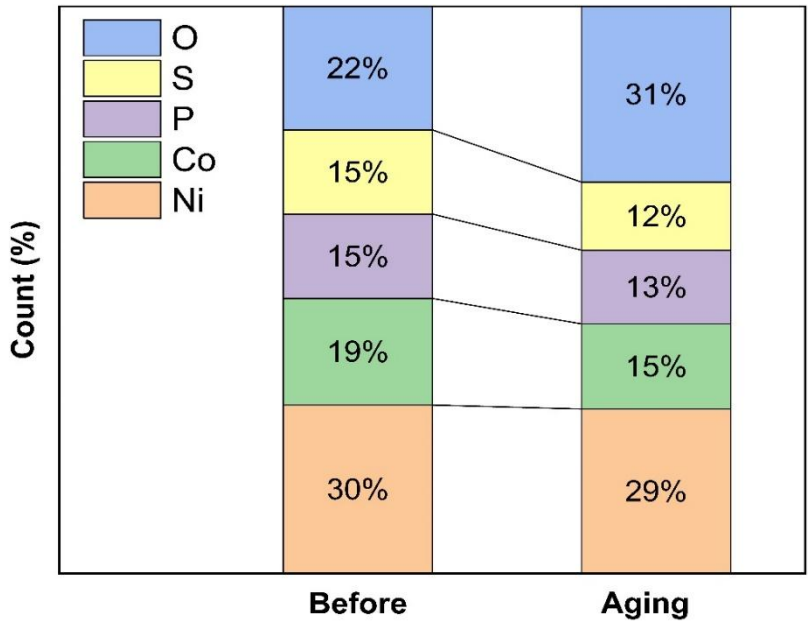

Fig. S22. The atomic ratio of CoNiP/NiS/NF heterostructure nanorods electrode before and after aging.

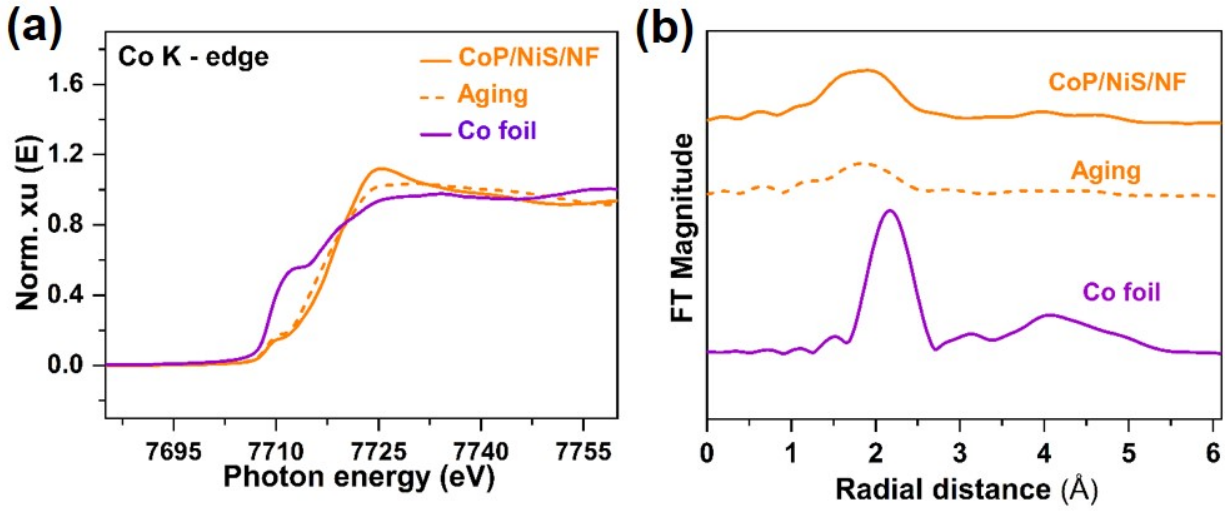

Fig. S23. (a-b), (Normalized XANES spectra and the Co K-edge for the k^3-weighted Fourier transform of EXAFS spectra for CoNiP/NiS/NF samples, respectively, before and after aging.

Table S1. Comparison of the electrocatalytic activity of CoNiP/NiS/NF to the recently reported noble-metal free HER catalysts in 1 M KOH.

Catalyst	**Current density ($mA\ cm^{-2}$)**	**Overpotential (mV)**	**Reference**
$NiMoO_x$/NiMoS/NF	10	38	[18]
CoNiP/NiS/NF	10	51	**Present work**
N-$NiMoO_4$/NiS_2/NF	10	57	[19]
CoP–$Ce_2(CO_3)_2O$/NF	10	85.2	[20]
P-$CoMoO_4$@NiCoP	10	66	[21]
CoP/NiCoP/NC	10	75	[22]
MoP/Ni_2P/NF	10	75	[23]
Ni_2P/Ni_3S_2/NF	10	80	[24]
Mo-NiP_x/NiS_y	10	85	[25]
$NiCo_{16-x}P_6$/NF	10	88	[26]
NiFeSP/NF	10	91	[27]
Ni_2P-Ru_2P/NF	10	101	[28]
NiFe LDH@NiCoP/NF	10	120	[29]
NiCoP@NiMn LDH/NF	10	NA	[30]
CoNiP/NiS/NF	100	110	**Present work**
NiCoP@NiMn LDH/NF	100	116	[30]
Co/CoMoN/NF	100	173	[31]
Mo-NiP_x/NiS_y	100	173	[25]

$NiMoO_x$/NiMoS/NF	100	186	[18]
NiFeSP/NF	100	186	[27]
MoP/Ni_2P/NF	100	191	[23]
Ni_2P-Ru_2P/NF	100	200	[28]
Ni_2P/Ni_3S_2/NF	100	210	[24]
CoP/NiCoP/NC	100	240	[22]
NiFe LDH@NiCoP/NF	100	250	[29]
N-$NiMoO_4$/NiS_2/NF	100	NA	[19]
$NiCo_{16-x}P_6$/NF	100	NA	[26]

Table S2. Comparison of stability of CoNiP/NiS/NF and other recently reported Pt-free electrocatalysts in 1 M KOH alkaline electrolyte on NF electrode.

Catalyst	**j (mA cm^{-2})**	**Stability (hr)**	**Reference**
CoNiP/NiS/NF	70	306	**Present work**
NiMo-NWs	50	40	[32]
Ni_2P/Ni_3S_2/NF	50	12	[33]
Mn-doped NiCoP	50	25	[34]
$Mo_2TiC_2T_x$MXene	50	24	[35]
NiFe-LDH/MoS_2–Ni_3S_2	50	24	[36]
H-CoS_x@NiFe LDH	10	100	[37]
NiFe-LDH@Mo–NiS_2–NiS	10	20	[38]
CO@NiFe-LDH	50	20	[39]
$Ni_{0.67}Co_{0.33}/Ni_3S_2$	50	25	[40]
Co_xP–Fe_2P	10	100	[41]
CoN/Ni $(OH)_2$	20	40	[42]
Ni-FeS_2-0.5	10	15	[43]
Ni-FeOx/$FeNi_3$	50	280	[44]
P-$CoMoO_4$@NiCoP	10	60	[45]
ZnCo/MoS2eCo_3S_4	50	48	[46]
NiFeP	10	135	[47]

Table S3. Calculated H* and *OH adsorption energy at different adsorption sites.

ΔG (eV)	Sites	ΔG -H* (eV)	ΔG -OH* (eV)
Ni_3S_2	Ni-Ni	0.796	2.205
	S	0.296	1.488
Ni_8P_3	Ni-P3	0.095	0.79
	Ni-Ni	-0.413	0.27
	P	0.235	0.60
CoP	Co	0.324	1.525
	P	0.002	0.175
CoP /Ni_3S_2	Co	0.427	0.427
	P	-0.032	-0.121
Ni_8P_3/Ni_3S_2	P	0.068	1.143

References

1. G. Kresse and J. Hafner, *Phys. Rev. B* 1993, **47**, 558-561.
2. J. P. Perdew, K. Burke and M. Ernzerhof, *Phys. Rev. Lett.* , 1996, **77**, 3865-3868.
3. G. Kresse and D. Joubert, *Phys. Rev. B Condens. Matter*, 1999, **59**, 1758-1775.
4. S. Grimme, J. Antony, S. Ehrlich and H. Krieg, *J. Chem. Phys.*, 2010, **132**, 154104.
5. S. Grimme, S. Ehrlich and L. Goerigk, *J. Comput. Chem.*, 2011, **32**, 1456-1465.
6. R. Zhang, X. Wang, S. Yu, T. Wen, X. Zhu, F. Yang, X. Sun, X. Wang and W. Hu, *Adv Mater*, 2017, **29**, 1605502.
7. M. Jin, X. Zhang, R. Shi, Q. Lian, S. Niu, O. Peng, Q. Wang and C. Cheng, *Appl. Catal. B*, 2021, **296**, 120350.
8. E. A. Moges, C.-Y. Chang, W.-H. Huang, K. Lakshmanan, Y. A. Awoke, C.-W. Pao, M.-C. Tsai, W.-N. Su and B. J. Hwang, *Adv. Funct. Mater.*, 2022, **32**, 2206887.
9. P. Ding, H. Song, J. Chang and S. Lu, *Nano Res.*, 2022, **15**, 7063-7070.
10. Y. Liu, Y. Bai, W. Yang, J. Ma and K. Sun, *Electrochim. Acta*, 2021, **367**, 137534.
11. J. Yang, H. Liu, W. N. Martens and R. L. Frost, *J. Phys. Chem. C*, 2010, **114**, 111-119.
12. J.-C. Kim and D.-W. Kim, *Int. J. Energy Res.*, 2022, **46**, 13035-13043.
13. H. Wang, Y. Zhou and S. Tao, *Appl. Catal. B*, 2022, **315**, 121588.
14. J. Nie, J. Shi, T. Huang, M.-Y. Xie, Z.-Y. Ouyang, M.-H. Xian, G.-F. Huang, H. Wan, W. Hu and W.-Q. Huang, *Adv. Funct. Mater.*, 2024, **n/a**, 2314172.
15. P. Li, W. Li, S. Zhao, Y. Huang, S. Tian and X. Huang, *J. Chem. Eng.*, 2022, **429**, 132557.
16. M. Gong, W. Zhou, M.-C. Tsai, J. Zhou, M. Guan, M.-C. Lin, B. Zhang, Y. Hu, D.-Y. Wang, J. Yang, S. J. Pennycook, B.-J. Hwang and H. Dai, *Nat. Commun.*, 2014, **5**, 4695.

17. D. Liu, H. Ai, M. Chen, P. Zhou, B. Li, D. Liu, X. Du, K. H. Lo, K.-W. Ng, S.-P. Wang, S. Chen, G. Xing, J. Hu and H. Pan, *Small*, 2021, **17**, 2007557.
18. P. Zhai, Y. Zhang, Y. Wu, J. Gao, B. Zhang, S. Cao, Y. Zhang, Z. Li, L. Sun and J. Hou, *Nat. Commun.*, 2020, **11**, 5462.
19. L. An, J. Feng, Y. Zhang, R. Wang, H. Liu, G.-C. Wang, F. Cheng and P. Xi, *Adv. Funct. Mater.*, 2019, **29**, 1805298.
20. L. Wang, M. Huang, M. Gao, T. T. Isimjan and X. Yang, *Mater. Chem. Front.*, 2023, **7**, 2628-2636.
21. N. You, S. Cao, M. Huang, X. Fan, K. Shi, H. Huang, Z. Chen, Z. Yang and W. Zhang, *NMS*, 2023, **5**, 278-286.
22. R. Boppella, J. Tan, W. Yang and J. Moon, *Adv. Funct. Mater.*, 2019, **29**, 1807976.
23. C. Du, M. Shang, J. Mao and W. Song, *J. Mater. Chem.*, 2017, **5**, 15940-15949.
24. L. Zeng, K. Sun, X. Wang, Y. Liu, Y. Pan, Z. Liu, D. Cao, Y. Song, S. Liu and C. Liu, *Nano Energy*, 2018, **51**, 26-36.
25. J. Wang, M. Zhang, G. Yang, W. Song, W. Zhong, X. Wang, M. Wang, T. Sun and Y. Tang, *Adv. Funct. Mater.*, 2021, **31**, 2101532.
26. Y. Zhao, J. Zhang, Y. Xie, B. Sun, J. Jiang, W.-J. Jiang, S. Xi, H. Y. Yang, K. Yan, S. Wang, X. Guo, P. Li, Z. Han, X. Lu, H. Liu and G. Wang, *Nano Lett.*, 2021, **21**, 823-832.
27. Y. Xin, X. Kan, L.-Y. Gan and Z. Zhang, *ACS nano*, 2017, **11**, 10303-10312.
28. S. Yang, J.-Y. Zhu, X.-N. Chen, M.-J. Huang, S.-H. Cai, J.-Y. Han and J.-S. Li, *Appl. Catal., B*, 2022, **304**, 120914.
29. H. Zhang, X. Li, A. Hähnel, V. Naumann, C. Lin, S. Azimi, S. L. Schweizer, A. W. Maijenburg and R. B. Wehrspohn, *Adv. Funct. Mater.*, 2018, **28**, 1706847.

30. P. Wang, J. Qi, X. Chen, C. Li, W. Li, T. Wang and C. Liang, *ACS Appl. Mater. Interfaces*, 2020, **12**, 4385-4395.
31. H. Ma, Z. Chen, Z. Wang, C. V. Singh and Q. Jiang, *J. Adv. Sci.*, 2022, **9**, 2105313.
32. M. Fang, W. Gao, G. Dong, Z. Xia, S. Yip, Y. Qin, Y. Qu and J. C. Ho, *Nano Energy*, 2016, **27**, 247-254.
33. Y. Li, H. Zhang, M. Jiang, Q. Zhang, P. He and X. Sun, *Adv. Funct. Mater.*, 2017, **27**, 1702513.
34. X. Yu, S. Xu, Z. Wang, X. Cheng, Y. Du, G. Chen, X. Sun and Q. Wu, *Nanoscale*, 2021, **13**, 11069-11076.
35. J. Wang, P. He, Y. Shen, L. Dai, Z. Li, Y. Wu and C. An, *Nano Res.*, 2021, **14**, 3474-3481.
36. S. Wang, X. Ning, Y. Cao, R. Chen, Z. Lu, J. Hu, J. Xie and A. Hao, *Inorg. Chem.*, 2023, DOI: 10.1021/acs.inorgchem.3c00425.
37. Y. J. Lee and S.-K. Park, *Small*, 2022, **18**, 2200586.
38. Y. Li, T. Dai, Q. Wu, X. Lang, L. Zhao and Q. Jiang, *Mater. Today Energy*, 2022, **23**, 100906.
39. H. Shi, K. Yang, F. Wang, Y. Ni and M. Zhai, *CrystEngComm*, 2021, **23**, 7141-7150.
40. Z. Wu, Y. Feng, Z. Qin, X. Han, X. Zheng, Y. Deng and W. Hu, *Small*, 2022, **18**, 2106904.
41. D. Li, C. Zhou, R. Yang, Y. Xing, S. Xu, D. Jiang, D. Tian and W. Shi, *ACS Sustain. Chem. Eng.*, 2021, **9**, 7737-7748.
42. Y. Cheng, F. Liao, H. Dong, H. Wei, H. Geng and M. Shao, *J. Power Sources*, 2020, **480**, 229151.
43. Z. Tan, L. Sharma, R. Kakkar, T. Meng, Y. Jiang and M. Cao, *Inorg. Chem.*, 2019, **58**, 7615-7627.

44. L. Trotochaud, J. K. Ranney, K. N. Williams and S. W. Boettcher, *J. Am. Chem. Soc.*, 2012, **134**, 17253.

45. N. You, S. Cao, M. Huang, X. Fan, K. Shi, H. Huang, Z. Chen, Z. Yang and W. Zhang, *J. Nanomater.*, 2021.

46. J. Jiang, H. Cong, X. Huang, R. Sun, Y. Li, W. Xu, H. Wang and S. Han, *Int. J. Hydrog.*, 2022, **47**, 2947-2957.

47. J. Cen, L. Wu, Y. Zeng, A. Ali, Y. Zhu and P. K. Shen, *ChemCatChem*, 2021, **13**, 4602-4609.